A Simultaneous Wideband Calibration for Digital Beamforming Arrays at Short Distances [Measurements Corner]

Ji, Yilin; Nielsen, Jesper Ødum; Fan, Wei

Published in:
I E E E Antennas and Propagation Magazine

DOI (link to publication from Publisher):
10.1109/MAP.2021.3069244

Publication date:
2021

Document Version
Accepted author manuscript, peer reviewed version

Simultaneous Wideband Calibration for Digital Beamforming Array at Short Distance

Yilin Ji, Jesper Ødum Nielsen, and Wei Fan

***Abstract*—Massive multiple-input multiple-output (MIMO) is seen as an essential feature for the fifth-generation (5G) communication systems. To ensure the array performance for beamforming or nulling, it is important to conduct array calibration beforehand. Since 5G massive MIMO base stations (BSs) are expected to be highly integrated, i.e. the antenna arrays are directly integrated with the transceiver front ends, there may be no antenna connectors reserved for calibration purpose. In this case, array calibration will be done fully over-the-air (OTA). In this work, we propose a fast and short-distance OTA calibration method for massive MIMO BSs based on digital beamforming structures. Specifically, the correlation-based sounding technique is utilized for simultaneous measurements, and phase deviation due to the spherical wavefront at short distance is corrected with the known propagation geometry. Moreover, a multipath cancellation scheme is adopted to improve the calibration accuracy. An experiment is conducted in an open laboratory environment to assess the validity and robustness of the proposed calibration method.**

***Index Terms*—Array calibration, correlation-based channel sounding, massive MIMO, and multipath cancellation.**

I. Introduction

A. Background

Massive multiple-input multiple-output (MIMO) is seen as an enabling technology for fifth-generation (5G) communication systems [1]. Future base stations (BSs) featuring massive MIMO technology are expected to be equipped with a large number of antennas with digital beamforming structures, where signals of all channels are independently accessible. The array radiation pattern can be controlled via setting proper complex weights to the antenna elements to, e.g. form a beam in a desired direction to overcome the unfavourable propagation loss, or to form a null in an interference signal direction to suppress unwanted signals [2]. In addition, spatial multiplexing can also be utilized to serve multiple users simultaneously over the same time and frequency resource with various precoding schemes, which enlarges the network capacity.

The use of beamforming and nulling relies on accurate control of the signal radiated from each antenna element [3]. However, the responses of radio chains of real BS products vary due to manufacturing or assembling uncertainty. Therefore, it is necessary to calibrate the massive MIMO BSs to align the amplitude and phase across different radio chains. This is mandatory in production testing before product roll-out to ensure that the performance of the systems can meet the expectation.

5G massive MIMO BSs are expected to be highly integrated [4], e.g. the antenna arrays are directly integrated with the transceiver front ends. Therefore, there may be no antenna connectors reserved for calibration purpose, and the radio chains and the antenna arrays need to be calibrated as a whole over-the-air (OTA) due to the lack of antenna connectors [5], [6].

B. Problem statement

The objective of the calibration is to obtain the relative far-field array response. Traditionally, the measurement is done in the far field of the test array. Relative array responses are measured with continuous wave (CW) signals for each antenna element sequentially, i.e. one antenna element in the array at a time. However, when it comes to calibration for massive MIMO systems, several challenges may arise.

Firstly, due to a large number of antenna elements in the array, it will take a huge amount of time to calibrate sequentially. Therefore, it is preferable to calibrate all antenna elements simultaneously to save time.

Secondly, when the array aperture becomes large, the corresponding minimum far-field distance (i.e. the Fraunhofer distance) grows significantly. Considering that array calibration is usually conducted in anechoic chambers, a large minimum far-field distance leads to a large chamber, which can be very expensive. On the other hand, when the probe antenna is placed too far away from the test array, the link budget might not be big enough to ensure a reliable calibration result. Therefore, calibration in the near field of test arrays is preferable, but somehow the far-field responses should be obtained.

Thirdly, even if the calibration is conducted in an anechoic chamber, non-negligible reflections in the test environment might still exist. In other words, the quiet zone in the chamber is not sufficiently anechoic. Therefore, some effective multipath cancellation is needed in the case where the test environment is not sufficiently anechoic.

Fourthly, ultra-wideband signals, e.g. with 400 MHz bandwidth, are expected to be used in 5G new radio [7]. A wideband array calibration method is needed in contrast to single-tone calibration.

Lastly, when antenna arrays are integrated with transceiver front ends, which also include baseband units, CW signals can not be used for calibration anymore. In this case, modulated signals supported by the baseband unit shall be used instead.

The authors are with Antennas, Propagation and Millimeter-wave Systems (APMS) section at Department of Electronic Systems, Aalborg University, Aalborg, Denmark, 9220. Email: {yilin, jni, wfa}@es.aau.dk. (Corresponding author: Wei Fan)

Overall, there is a strong need for fast, wideband, and compact array calibration methods for massive MIMO systems in production testing.

C. State-of-the-art

Many OTA array calibration methods can be found in the literature. The rotating element electric field vector method (REV) [8], the mutual coupling method [9], and the phase-match method [10], calibrate antenna elements sequentially in the far field, which leads to long measurement time. Simultaneous multi-element calibration methods include the control circuit encoding (CCE) method [11], and the synthetic array calibration (SAC) method [12], both of which are based on the matrix inversion principle. However, all these methods are designed for narrowband array systems with a small number of antenna elements, and the far-field condition is required.

Near-field methods include the plane wave generator (PWG) [13], the compact antenna test range (CATR) [14], and the near field to far field transformation (NF-FF) [15]. The former two methods generate a plane wave in the quiet zone close to the probe antennas. The third one needs a number of samples on a regular grid enclosing the test array, and the required number is proportional to the array aperture. However, these methods are sequential calibration methods, and the cost of those setups is typically high. Moreover, these methods are designed for CW signals.

D. Contribution

In this paper, the correlation-based sounding technique is used for parallel wideband array calibration. This technique is commonly used in the traditional channel sounding area, and it has been proposed for array calibration in [16], [17]. In this work, we try to adapt this method for calibrating arrays integrated with radio chains over-the-air in the same fashion as required in [4]. Since the responses of all chains can be measured simultaneously, the calibration time is reduced significantly compared to sequential calibration methods. Moreover, multiple channel snapshots can be measured rapidly with the proposed setup, and further averaged to achieve a higher signal-to-noise ratio (SNR), and hence a higher calibration accuracy.

The proposed method utilizes a single probe antenna placed in the near field of the test array, and phase compensation according to propagation geometry is performed to account for the spherical wavefront. In addition, a multipath cancellation step is taken to remove potential reflections in the test environment. The multipath components are estimated with the expectation-maximization algorithm [18] which is typically used for channel estimation, and only the strongest path is kept for calibration. The proposed calibration framework offers short calibration time in a compact measurement setup, which is highly valuable for the industry.

The rest of the paper is organized as follows: In Section II, we define the signal model for the array calibration problem. The used method to cope with reflections in test environments, the effect of calibration in the near field of the test array, and the sounding principle are also discussed in this section. In Section III, we introduce the validation experiment. Section IV shows the results obtained from our calibration method. Lastly, Section V concludes the paper.

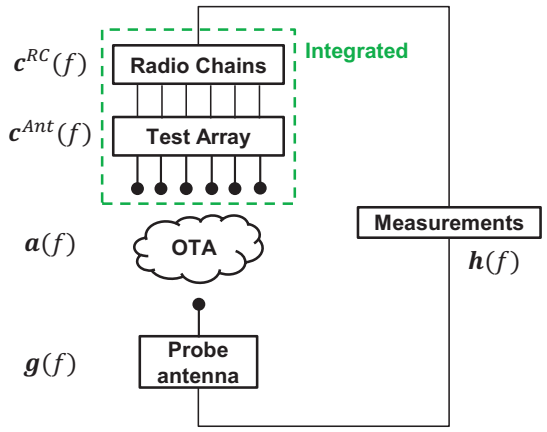

Fig. 1. Block diagram of the proposed array calibration setup.

II. Massive MIMO Array Calibration

A. Signal model

The block diagram of the proposed array calibration setup is shown in Fig. 1. The responses of the radio chains, the test array, the OTA propagation channel, and the probe antenna at the frequency f are denoted as $\boldsymbol{c}^{RC}(f)$, $\boldsymbol{c}^{Ant}(f)$, $\boldsymbol{a}(f)$, and $\boldsymbol{g}(f)$, respectively. The total link response is denoted as $\boldsymbol{h}(f)$. All of those terms are complex-valued M-entry vectors with M being the number of antenna elements in the test array. For brevity, we drop the frequency dependency in those responses hereafter unless noted otherwise.

Let us assume the calibration is done in free space. This is usually assumed when the calibration is done in anechoic chambers where reflections are small and negligible. The mth entry, with $m \in [1, M]$, of the total link response vector $\boldsymbol{h}$ can be expressed as

$$h_m = c_m^{RC} \cdot c_m^{Ant}(\theta + \Delta\theta_m) \cdot a_m \cdot g(\phi + \Delta\phi_m), \qquad (1)$$

where $c_m^{Ant}(\cdot)$ and $g(\cdot)$ are the antenna radiation pattern of the mth test array element and the probe antenna, respectively. The angle $(\theta + \Delta\theta_m)$ is the incident angle at the mth element, with θ being the angle at the center of the test array, and $\Delta\theta_m$ the angle offset for the mth element. Similarly, $(\phi + \Delta\phi_m)$ is the incident angle at the probe antenna from the mth test array element, with ϕ being the angle from the test array center, and $\Delta\phi_m$ the angle offset for the mth element. Note that the angles here can be replaced with directions when both azimuth and elevation are considered. The sketch describing the incident angles in the respective local coordinate systems is shown in Fig. 2. The response a_m can be modelled as

$$a_m = \frac{\lambda}{4\pi d_m} \cdot \exp\left(-j\frac{2\pi}{\lambda} d_m\right), \qquad (2)$$

with λ being the wavelength depending on f, and d_m being the distance between the mth test antenna element and the probe antenna. Note that the probe antenna is usually put in

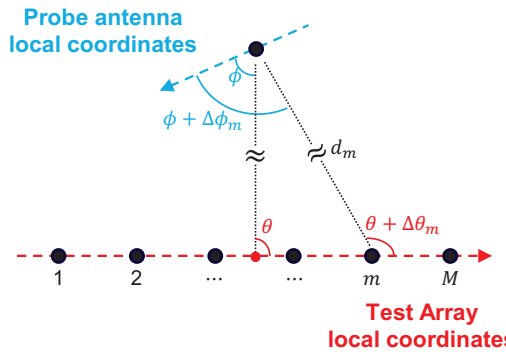

Fig. 2. Sketch of the local coordinate systems for the test array and the probe antenna.

the boresight direction of the test array, i.e. $\theta = \theta_{bore}$, for amplitude and phase alignment applications for radio chains.

When the probe antenna is placed in the far field of the test antenna array, the following approximations can be made: $\Delta\theta_m = \Delta\phi_m = 0$ and $|a_m| = |a_1|$ for all $m \in [1, M]$. In this case, we define the relative far-field array response $\tilde{\boldsymbol{h}}$ for the direction θ as

$$\tilde{\boldsymbol{h}} = \frac{\boldsymbol{h}}{h_{m'}}, \tag{3}$$

with $m' \in [1, M]$ being the index of the reference antenna element, and the mth entry of $\tilde{\boldsymbol{h}}$ reads

$$\tilde{h}_m = \frac{c_m^{RC} \cdot c_m^{Ant}(\theta)}{c_{m'}^{RC} \cdot c_{m'}^{Ant}(\theta)} \cdot \exp\left(-j\frac{2\pi}{\lambda}(d_m - d_{m'})\right). \tag{4}$$

Note that obtaining the far-field relative array response $\tilde{\boldsymbol{h}}$ in (3) is the objective of array calibration.

B. Multipath cancellation

When the test environment is not sufficiently anechoic, it may not be appropriate to assume single-path propagation anymore. Therefore, the signal model in (1) needs to be modified for the multipath case as

$$\begin{aligned} h_m^{\Sigma} &= \sum_{l=1}^{L} h_{m,l} \\ &= \sum_{l=1}^{L} \left\{ c_m^{RC} \cdot c_m^{Ant}(\theta_l + \Delta\theta_{m,l}) \cdot a_{m,l} \cdot g(\phi_l + \Delta\phi_{m,l}) \right\}, \end{aligned} \tag{5}$$

where $l \in [1, L]$ is the path index, and L is the total number of paths in the test environment. The definitions for θ_l, $\Delta\theta_{m,l}$, ϕ_l, and $\Delta\phi_{m,l}$ remain almost the same as their respective corresponding terms in (1), except that they are now for the lth path. The major change happens to the expression of the OTA propagation response $a_{m,l}$, which is not a simple extension of a_m given in (2) due to reflections and diffractions. However, we can expect that the response $a_{m,l}$ corresponding to the line-of-sight (LoS) path is still ruled by (2). Therefore, if we can estimate the link response for the LoS path, and use that for the calibration, i.e. dropping the path index l thereafter, the multipath problem degenerates to a single-path problem, and the derivation given in Section II-A can be reused.

In the channel estimation field, there are various algorithms developed for estimating multipath components [18]–[21]. Multipath components can be decomposed from the fading channel via those algorithms in different domains, such as the delay, angle, and Doppler frequency domain. However, since the test environment is typically static, and the relative far-field array response, which is our objective, is unknown beforehand, the decomposition can only be done in the delay domain.

The delay domain is the Fourier transform dual to the frequency domain. Therefore, wideband measurements are required to perform multipath cancellation in this case. The intrinsic delay resolution is inversely proportional to the signal bandwidth. When the difference of the delay between potential multipaths and the LoS path is smaller than this resolution, super-resolution iterative algorithms, such as the expectation-maximization algorithm [18], are preferred for the estimation. Nonetheless, if the delay difference is much larger than the intrinsic resolution, time gating can also be used to remove multipaths from the measurements.

C. Effect of incident angle offset on antenna radiation pattern

In order to make the calibration setup compact and to fulfil the link budget, the probe antenna needs to be placed in the near field of the test antenna array. In this case, the approximations made in Section II-A, i.e. $\Delta\theta_m = \Delta\phi_m = 0$ and $|a_m| = |a_1|$ for all $m \in [1, M]$, do not hold. As a result, the mth entry of the relative near-field array response $\hat{\boldsymbol{h}}$ for the direction θ reads (c.f. (4))

$$\begin{aligned} \hat{h}_m = &\overbrace{\frac{c_m^{RC} \cdot c_m^{Ant}(\theta + \Delta\theta_m)}{c_{m'}^{RC} \cdot c_{m'}^{Ant}(\theta + \Delta\theta_{m'})}}^{\text{test array}} \cdot \overbrace{\frac{g(\phi + \Delta\phi_m)}{g(\phi + \Delta\phi_{m'})}}^{\text{probe}} \\ &\underbrace{\cdot \frac{d_{m'}}{d_m} \cdot \exp\left(-j\frac{2\pi}{\lambda}(d_m - d_{m'})\right)}_{\text{propagation}}, \end{aligned} \tag{6}$$

where m' is, again, the index of the reference element. One can see that $\hat{h}_m$ converges to $\tilde{h}_m$ with the increase of d_m. Note that (6) is valid only if the mutual coupling between the test array elements is negligible. Otherwise, the antenna radiation pattern $c_m^{Ant}(\cdot)$ shall vary with the distance as well.

Given the distance d_m for all $m \in [1, M]$, the term in (6) corresponding to the propagation can be calculated accordingly, and it can be compensated so as to be equivalent to that in (4). Moreover, the angle offset $\Delta\phi_m$ can be calculated according to the geometry of the calibration setup. Given the knowledge of antenna radiation pattern of the probe antenna, the term in (6) corresponding to the probe antenna pattern can also be compensated for.

The angle offset $\Delta\theta_m$ can also be calculated according to the geometry of the calibration setup. However, since the radiation patterns of the test array elements are not known beforehand, the term corresponding to the test array in (6) can not be corrected by any means. Therefore, there is still a deviation between $\hat{h}_m$ and $\tilde{h}_m$ after the probe pattern and

propagation compensation. The significance of the deviation depends on $\Delta\theta_m$ and c_m^{Ant} for all $m \in [1, M]$. Intuitively, a smaller $\Delta\theta_m$ (which is equivalent to a larger d_m) and a less variant c_m^{Ant} lead to a smaller deviation. In this work, this deviation is not treated, and it is inherent in the calibration results.

D. Channel sounding principle

A massive MIMO BS is expected to have a digital beamforming structure, where the data stream of each chain is independent and accessible. The underlying system structure is very similar to that of the conventional time-domain channel sounders [22], which offer parallel measurement capability for multiple chains. Therefore, it is very straightforward to use the channel sounding technique for digital beamforming array calibration. Moreover, due to the nature of direct sequence spread spectrum techniques, the test array can be calibrated over the frequency band of interest.

Each chain in the test array is fed with the so-called pseudo-noise (PN) sequence, the auto-correlation function of which approximates the Dirac delta function (i.e. the orthogonality). For the mth chain, the PN sequence at the delay $\tau \in [0, T]$ reads

$$x_m(\tau) = x_1(\tau - (m-1)\cdot\Delta T), \tag{7}$$

where T is the total duration of the PN sequence, and ΔT is the delay duration shifted between adjacent chains. The orthogonality can be represented as

$$x_m(\tau) \star x_1(\tau) = \delta(\tau - (m-1)\cdot\Delta T), \tag{8}$$

where $\star$ denotes the correlation operator, and $\delta(\cdot)$ the delta function. The received signal $y(\tau)$ by the probe antenna can be written as

$$y(\tau) = \sum_{m=1}^{M} x_m(\tau) * H_m(\tau) + n(\tau), \tag{9}$$

where $*$ denotes the convolution operator, $H_m(\tau)$ is the Fourier transform pair of $h_m(f)$, and $n(\tau)$ is the measurement thermal noise. By correlating $y(\tau)$ with $x_1(\tau)$, we obtain the composite impulse response $\underline{H}(\tau)$ consisting of the responses for all M chains

$$\begin{aligned}\underline{H}(\tau) &= y(\tau) \star x_1(\tau) \\ &= \sum_{m=1}^{M} H_m(\tau) * \delta(\tau - (m-1)\cdot\Delta T) + n'(\tau),\end{aligned} \tag{10}$$

where $n'(\tau)$ is the thermal noise averaged over time T. The response for the mth chain $H_m(\tau)$ can then be approximated by chopping $\underline{H}(\tau)$ into M blocks, each of which has the length ΔT

$$H_m(\tau) \approx \underline{H}(\tau + (m-1)\cdot\Delta T), \tag{11}$$

with $\tau \in [0, \Delta T]$. Note that $(M \cdot \Delta T)$ needs to be smaller than T, and ΔT needs to be larger than the maximum excess delay of the channel for all chains.

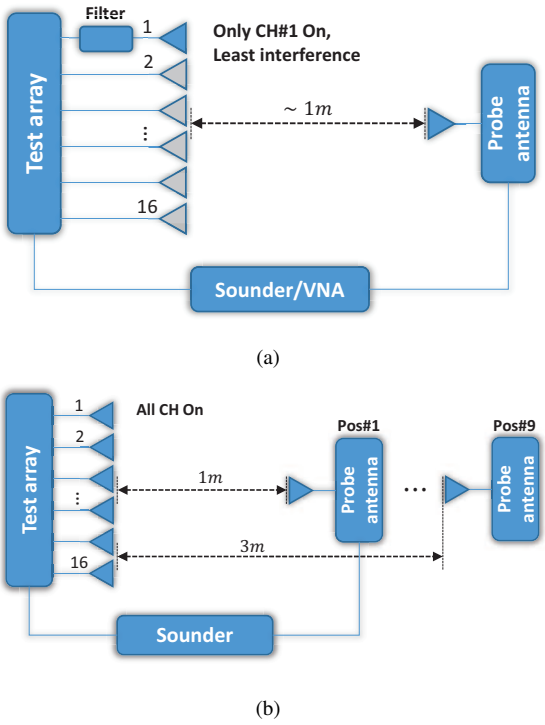

Fig. 3. Sketches for (a) measurement series 1, and (b) measurement series 2.

III. Measurement Description

A. Measurement System

A correlation-based channel sounder is used in the validation measurement to mimic the massive MIMO BS with digital beamforming structures [22]. Parallel transmission is realized with the individual signal generator in each transmitter chain. The PN sequence has a length of 4095 chips, and is modulated with binary phase-shift keying (BPSK). The modulated sequence is transmitted at 100 MHz (i.e. the signal bandwidth), and the receiver records 60 channel snapshots per second. The center frequency is set to 3.5 GHz. The transmitter side (the test array) is equipped with 16 antennas which forms a uniform linear array (ULA), and the receiver side has one antenna (the probe antenna). Vivaldi antennas of the same type are used on both sides. The antenna has about 45° half-power beam width (HPBW) and 11 dB gain. The inter-element spacing at the test array is 5 cm, which is slightly larger than the half wavelength (about 4.28 cm) at 3.5 GHz. The Fraunhofer distance of the test array under this setting is about 13 m. The transmitter and the receiver sides are synchronized.

B. Measurement Campaign

Two series of measurements are conducted for different purposes. The sketches for the two series are shown in Fig. 3. The first measurement series (Fig. 3(a)) is designed to check the stability and accuracy of the channel sounder in the amplitude and phase. In this series, the probe antenna is aligned to the center of the test array, and placed about 1 m away. We insert an external filter into one of the radio

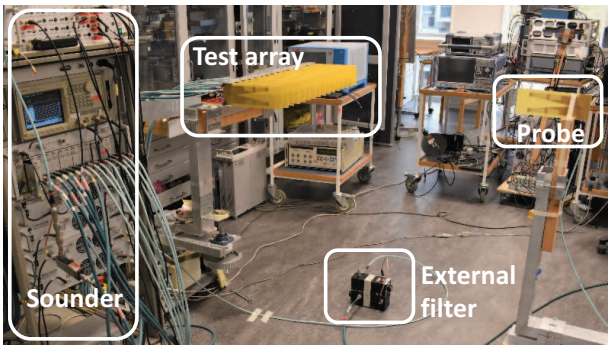

(a)

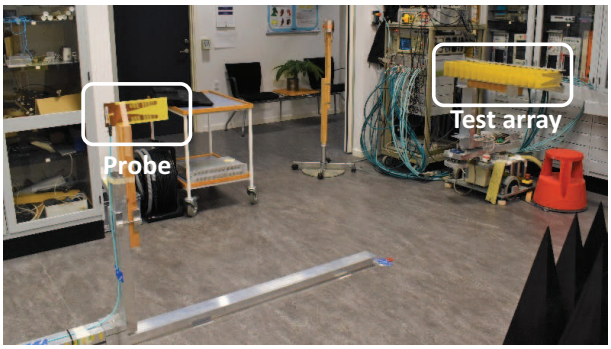

(b)

Fig. 4. Photos for the two measurement series, (a) measurement series 1 (b) measurement series 2. Both series are conducted in an open laboratory environment.

chains of the test array to measure the frequency response of the filter. The filter response is estimated by dividing the link response of the chain with the filter inserted over the link response without the filter inserted in the frequency domain. This approach is valid if the reflection that exists in the radio chain is negligible (impedance matched). During the measurement, only the chain with the external filter (CH#1) is turned on to have the least interference from the other chains. The measurement is repeated several times to obtain some statistics of the sounder performance. The filter response is also measured with a vector network analyzer (VNA) to compare with that measured with the sounder.

In the second measurement series, the external filter is removed and all 16 chains are turned on (Fig. 3(b)). The probe antenna is still aligned to the center of the test array but the distance is shifted from 1 m to 3 m with 25 cm per step, which leads to in total 9 positions (Pos#1 - Pos#9) for the probe antenna. At each position, the link response $\boldsymbol{h}$ is measured with the sounder. Note that all the measurement distances are smaller than the underlying Fraunhofer distance of the test array.

All measurements are conducted with a duration of 20 seconds, which leads to 1200 channel snapshots for each measurement. The resulting link responses are averaged over all those snapshots to achieve a higher SNR. Besides, all measurements are conducted in an open laboratory environment, where multipaths are expected to exist. Photos for the two measurement setups are shown in Fig. 4.

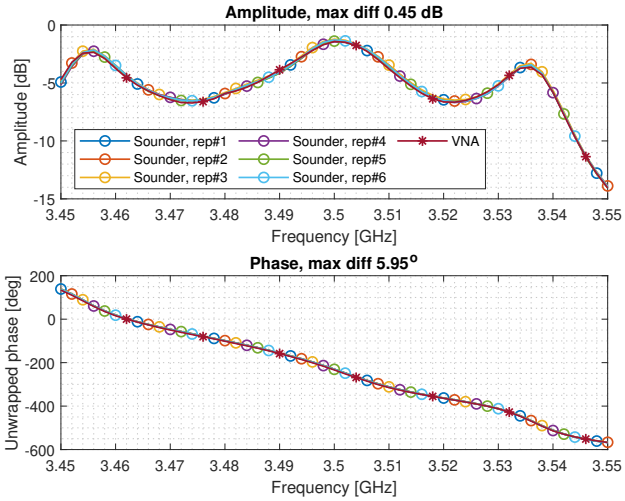

Fig. 5. The measured filter response from the first measurement series over the frequency band of interest, i.e. 100 MHz centered at 3.5 GHz.

TABLE I
RMSE OF THE SOUNDER MEASUREMENTS TO THE VNA MEASUREMENT

Rep#	1	2	3	4	5	6
Amplitude [dB]	0.13	0.16	0.20	0.15	0.13	0.15
Phase [deg]	2.57	2.77	2.95	1.95	2.09	2.11

IV. Measurement Results and Analysis

A. Measurement Series 1

The filter response obtained from the first series is shown in Fig. 5 in terms of the amplitude and phase. In total, the sounder measurement is repeated 6 times (Rep#1 - Rep#6). Note that we also flex the coaxial cable deliberately between the repetitions to include the cable effect on result stability. The maximum deviation over the considered frequency band for all the sounder measurements to the reference VNA measurement is 0.45 dB in amplitude and 5.95° in phase, which shows the capability of the sounder in wideband measurements. The root-mean-square error (RMSE) for each sounder measurement compared to the VNA measurement is listed in Table I, which shows the stability and accuracy of the sounder.

B. Measurement Series 2

1) Measured link responses: During the second series, a coupler is mounted on the first radio chain (CH#1), and the coupled signal is measured at the receiver side via a coaxial cable connecting the transmit antenna port to the receive antenna port. This cabled measurement characterizes the system responses of the radio chains of the sounder. Besides, the system response is also used later for path estimation for multipath cancellation in our case. For general commercial products without reserved antenna ports, the system response can be estimated with the pre-known internal filters responses. The resulting system response is shown in Fig. 6 in the delay and frequency domain.

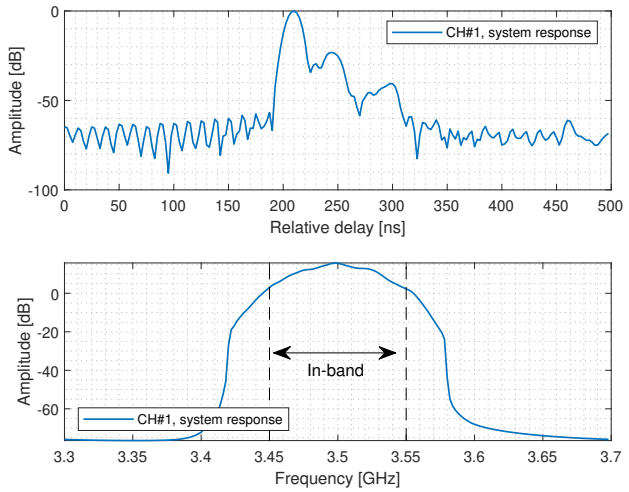

Fig. 6. The back-to-back response for the first radio chain (CH#1) (top) in the delay domain and (bottom) in the frequency domain.

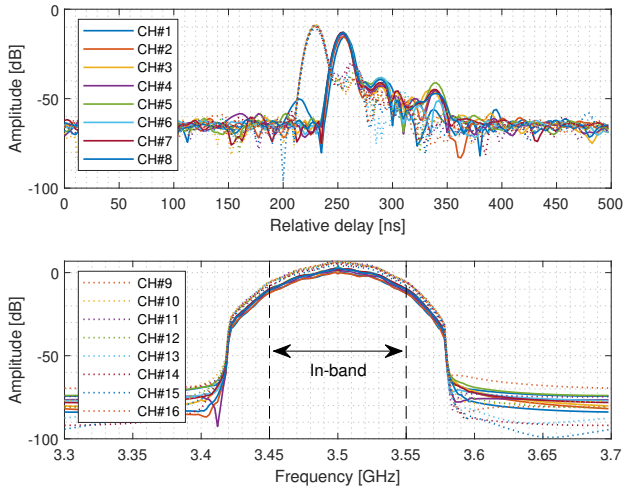

Fig. 7. The link responses for all 16 radio chains (CH#1 - CH#16) measured at Pos#1 (top) in the delay domain and (bottom) in the frequency domain.

The link responses for all 16 chains (CH#1 - CH#16) measured at Pos#1 in the delay and frequency domain is shown in Fig. 7. Different delays are set in the sounder between half of the chains (CH#1 - CH#8) and the other half (CH#9 - CH#16) in order to imitate possible delay difference in radio chains of real products. Comparing Fig. 7 with Fig. 6, the number of multipaths in the OTA propagation seems to be small for Pos#1, and the effect of multipath fading (frequency selectivity) on the measured link responses seems to be minor. This is somewhat contradictory to our expectation for the messy test environment shown in Fig. 4. However, since the antennas used in the experiment are directional (i.e. 45° HPBW Vivaldi antennas), potential multipaths might have been filtered out by the antenna radiation pattern. Therefore, this observation is reasonable, and further multipath cancellation may not be needed in this case. Nonetheless, in other cases where multipath fading is significant, multipath cancellation is still needed for a better calibration accuracy. Note that when the measurement is taken at a larger distance, such as Pos#7, Pos#8, and Pos#9, a relatively more significant effect of multipath fading can occur. In fact, as is shown later, the multipath cancellation scheme does help to improve the calibration accuracy at those positions.

2) Resulting relative array responses: Despite the multipath fading may be small in our measurement, the multipath cancellation scheme discussed in Section II-B is still performed to achieve a higher calibration accuracy. The multipath components are estimated with the expectation-maximization algorithm [18]. The system response shown in Fig. 6 is used as the basis function, i.e. the signal model for a single path, for the estimation. The frequency response of each chain is reconstructed with the estimated delay and complex amplitude of the strongest path for that chain with respect to the basis function.

In order to check the significance of the improvement, the resulting relative array responses without and with the multipath cancellation for 3.5 GHz are shown in the complex plane in Fig. 8 and Fig. 9, respectively. Different colors and markers represent different chains. The results of each chain for different measurement positions (Pos#1 - Pos#9) are connected with lines. The development of the results from Pos#1 to Pos#9 is indicated with the decreasing sizes of the markers.

For the results shown in Fig. 8(a) and Fig. 9(a) (i.e. the results before the propagation compensation), the trajectories of the relative array responses for those array elements close to the ends of the test array, such as CH#1, CH#2, CH#15, and CH#16, roughly fall on circles, which is caused by the spherical wavefront as the probe antenna is placed in the near field of the test array. Comparing Fig. 9(a) to Fig. 8(a), we can see the trajectories are more circular-shaped, which indicates that the relative array responses obtained with the multipath cancellation follow more closely our signal model in Section II-A.

For the results shown in Fig. 8(b) and Fig. 9(b) (i.e. the results after the propagation compensation), the trajectories of the relative array responses for all array elements tend to converge to their respective local clusters. Comparing Fig. 8(b) and Fig. 9(b), the local clusters for the case with the multipath cancellation seem to be slightly more compact, which indicates the marginal but noticeable improvement on the calibration accuracy when using the multipath cancellation.

Nevertheless, we can see that some of the trajectories of the relative array responses are still spreading out after the propagation compensation in Fig. 9(b), especially those corresponding to the elements close to the ends of the test array, e.g. CH#1, CH#2, CH#15, and CH#16. One possible cause for this is the incident angle offset discussed in Section II-C. When the probe antenna is placed at 1 m from the test array, the incident angle offset $\Delta\theta$ for the outmost elements, i.e. CH#1 and CH#16, is about 21°, which is very close to half of the HPBW of the test array antennas. Therefore, a more severe deviation to the true far-field relative array response can be expected.

Another possible cause is the variation of the antenna

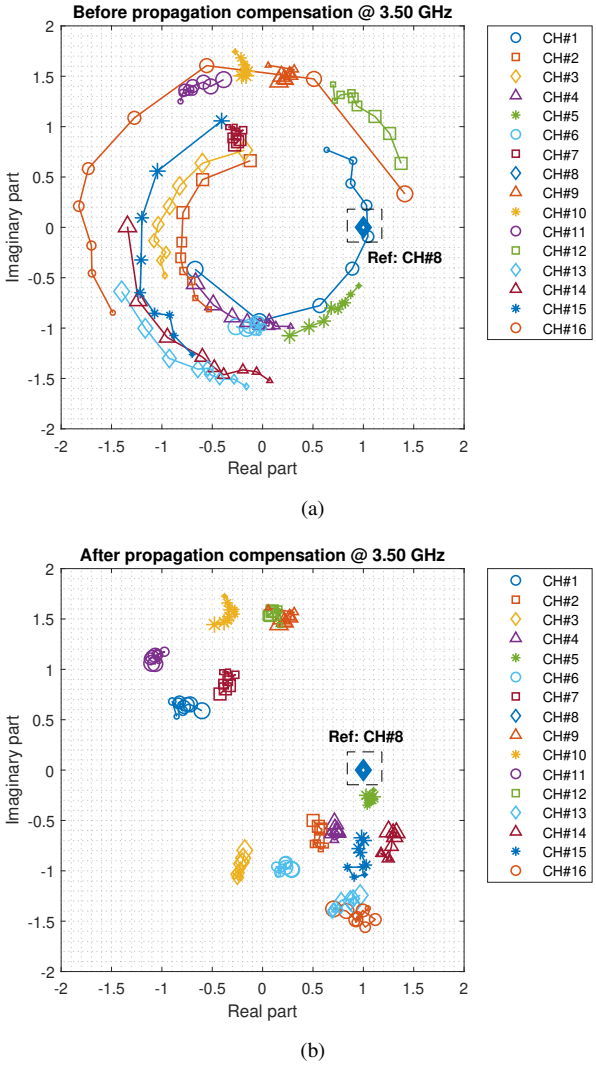

Fig. 8. The relative array responses referenced to the 8th test array element (CH#8) at 3.5 GHz (a) before the propagation compensation, and (b) after the propagation compensation, both without the multipath cancellation.

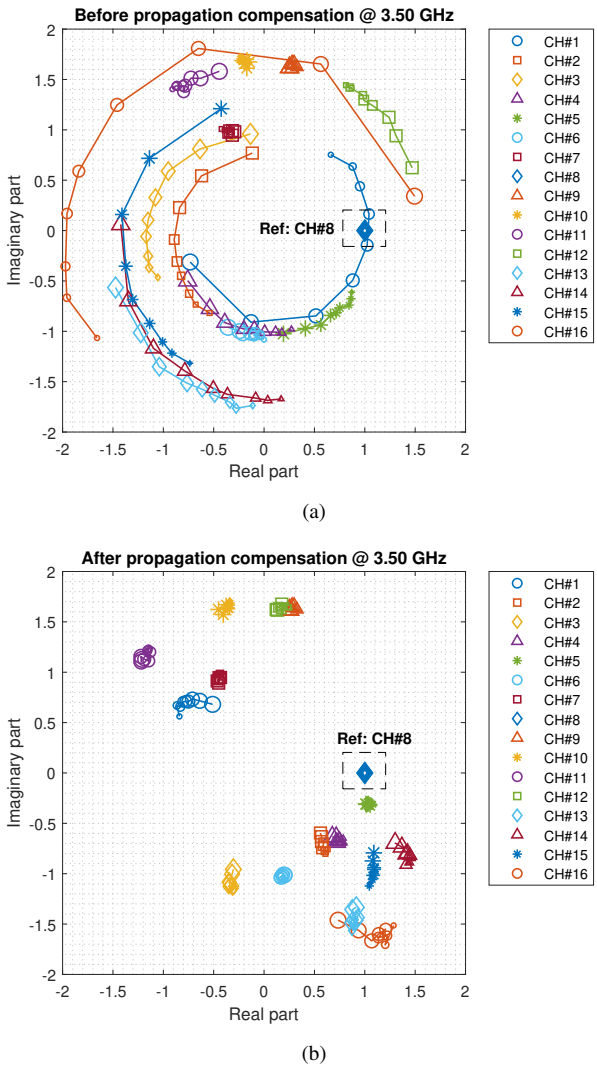

Fig. 9. The relative array responses referenced to the 8th test array element (CH#8) at 3.5 GHz (a) before the propagation compensation, and (b) after the propagation compensation, both with the multipath cancellation.

radiation pattern of the outmost elements in the test array. Since there are no additional dummy elements further outside the outmost active elements, the antenna radiation pattern of those elements differs from that of the elements in the central of the test array. This radiation pattern change on the outmost elements might aggravate the effect of the angle offset even further.

Fig. 10 shows the standard deviation of the amplitude and phase of the resulting relative array response for each radio chain with and without the multipath cancellation, i.e. from the results in Fig. 9(b) and Fig. 8(b), respectively. Since the 8th element (CH#8) is used as the reference, its amplitude and phase deviation are always 0 dB and 0°, respectively. The standard deviation of both the amplitude and phase is generally lower when the multipath cancellation is considered, which, again, shows the improvement of utilizing the multipath cancellation scheme for calibrating in open environments. Moreover, the standard deviation generally decreases as the radio chain index gets closer to the center of the test array,

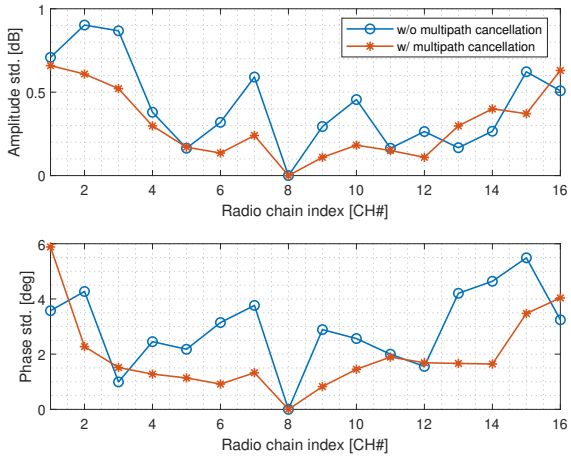

Fig. 10. The standard deviation (std.) of the (top) amplitude and (bottom) phase of the resulting relative array response with and without the multipath cancellation taking all measurement distances into account.

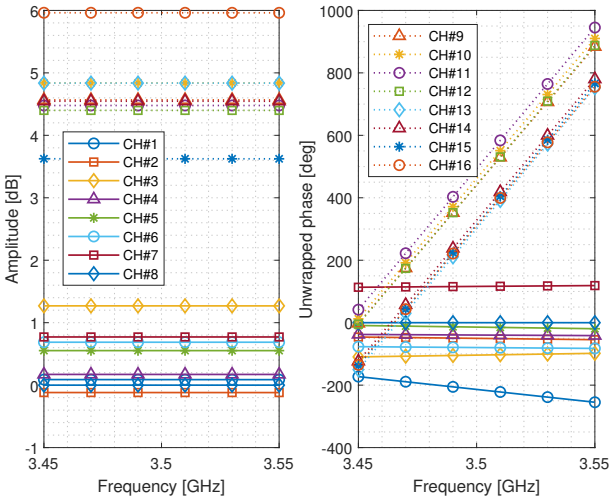

Fig. 11. The calibrated relative array response over the frequency band of interest, (left) the amplitude and (right) the phase. The 8th element in the test array (CH#8) is used as the reference element.

which is consistent with our discussion given before. Overall, the achieved standard deviation is below 1 dB and 6° for the amplitude and phase, respectively.

Finally, the resulting relative array response at Pos#9 after the multipath cancellation, which has the smallest incident angle offset effect (i.e. about 8° for the outmost elements), is used as the calibrated relative array response as shown in Fig. 11. Since the 8th element in the test array (CH#8) is used as the reference element, its amplitude and phase are always 0 dB and 0°, respectively, over the frequency band of interest. The relative amplitude response is flat for all chains since the same basis function, i.e. the system response shown in Fig. 6, is used for path estimation. The level of the amplitude response indicates the relative gain of each chain. The slopes of the phase responses in Fig. 11 correspond to the difference in delay between different chains and the reference chain CH#8 (see the top subplot in Fig. 7).

V. Conclusion

In this paper, we propose a wideband antenna array calibration method for massive MIMO systems. This method allows for array calibration at short distance, and it has the ability to cope with potential multipath fading in the test environment. All these features are very important when there are link budget and reflection issues for calibration. Moreover, all radio channels and array elements are calibrated simultaneously, which reduces the calibration time.

The proposed method is validated with an experiment conducted in an open laboratory environment. The results show the multipath cancellation scheme helps to improve the accuracy of the final calibrated relative array response. The experiment shows that it is possible to conduct array calibration without an anechoic chamber.

It is also shown that phase deviation due to the spherical wavefront in the near field can be corrected with the known propagation geometry. However, as pointed out in Section II-C, the calibration error due to the incident angle offset on test array element pattern still remains in the final result. To study how significant the error could be, a reference far-field array response needs to be measured in an anechoic chamber for comparison in the future work. Nevertheless, it is expected that a smaller incident angle offset would lead to smaller calibration error contributed from the variation of the element pattern within that angular region.

Acknowledgment

The authors would like to thank Mr. Kim Olesen and Mr. Kristian Bank for their help with the practical measurements.

References

[1] J. J. G. Andrews, S. Buzzi, W. Choi, S. V. S. Hanly, A. Lozano, A. A. C. K. Soong, and J. J. C. Zhang, "What will 5G be?" *IEEE Journal on Selected Areas in Communications*, vol. 32, no. 6, pp. 1065–1082, 2014.

[2] A. W. Mbugua, W. Fan, Y. Ji, and G. F. Pedersen, "Millimeter wave multi-user performance evaluation based on measured channels with virtual antenna array channel sounder," *IEEE Access*, vol. 6, pp. 12 318–12 326, 2018.

[3] H. Krim and M. Viberg, "Two decades of array signal processing research: The parametric approach," *IEEE Signal Processing Magazine*, vol. 13, no. 4, pp. 67–94, 1996.

[4] 3GPP, "Base Station (BS) conformance testing Part 2: Radiated conformance testing," Tech. Rep. 3GPP TS 38.141-2 V16.1.0, 2019.

[5] M. Rumney, "Testing 5G: Time to Throw Away the Cables," *MICROWAVE JOURNAL*, vol. 59, no. 11, pp. 10–18, 2016.

[6] W. Fan, P. Kyosti, M. Rumney, X. Chen, and G. F. Pedersen, "Over-the-air radiated testing of millimeter-wave beam-steerable devices in a cost-effective measurement setup," *IEEE Communications Magazine*, vol. 56, no. 7, pp. 64–71, 2018.

[7] 3GPP, "5G; NR; Base Station (BS) radio transmission and reception," Tech. Rep. 3GPP TS 38.104 V15.2.0, 2019.

[8] T. Takahashi, Y. Konishi, S. Makino, H. Ohmine, and H. Nakaguro, "Fast measurement technique for phased array calibration," *IEEE Transactions on Antennas and Propagation*, vol. 56, no. 7, pp. 1888–1899, 2008.

[9] Y. Neidman, R. Shavit, and A. Bronshtein, "Diagnostic of phased arrays with faulty elements using the mutual coupling method," *IET Microwaves, Antennas & Propagation*, vol. 3, no. 2, pp. 235–241, 2009.

[10] C. N. Hu, "A Novel Method for Calibrating Deployed Active Antenna Arrays," *IEEE Transactions on Antennas and Propagation*, vol. 63, no. 4, pp. 1650–1657, 2015.

[11] S. D. Silverstein, "Application of orthogonal codes to the calibration of active pahsed array antennas for communications satellites," *IEEE Transactions on Signal Processing*, vol. 47, no. 1, pp. 206–218, 1997.

[12] W. P. M. N. Keizer, "Synthetic Array Approach," *IEEE Transactions on Antennas and Propagation*, vol. 59, no. 11, pp. 4115–4122, 2011.

[13] O. M. Bucci, M. D. Migliore, G. Panariello, and D. Pinchera, "Plane-wave generators: Design guidelines, achievable performances and effective synthesis," *IEEE Transactions on Antennas and Propagation*, vol. 61, no. 4, pp. 2005–2018, 2013.

[14] M. Nel, J. Joubert, and J. W. Odendaal, "The measurement of complex antenna transfer functions for ultra-wideband antennas in a compact range [measurements corner]," *IEEE Antennas and Propagation Magazine*, vol. 56, no. 6, pp. 163–170, 2014.

[15] J. Hald and F. Jensen, *Spherical near-field antenna measurements*. Iet, 1988, vol. 26.

[16] K. S. Lyalin, D. V. Prikhodko, and V. V. K. Mrds, "Approach to Use Pseudo-Noise Sequences in Inner Calibration System of Active Phased Antenna Arrays," in *2016 IEEE NW Russia Young Researchers in Electrical and Electronic Engineering Conference (EIConRusNW)*, 2016, pp. 425–427.

[17] K. S. Lyalin, D. V. Prikhodko, V. V. Kurganov, M. S. Khasanov, and V. V. Chistukhin, "Approach to Use Pseudo-noise Calibration Method for Wideband Calibration of Antenna Arrays," in *2017 IEEE Conference of Russian Young Researchers in Electrical and Electronic Engineering (EIConRus)*, 2017, pp. 1257–1260.

[18] B. H. Fleury, M. Tschudin, R. Heddergott, D. Dahlhaus, and K. I. Pedersen, "Channel parameter estimation in mobile radio environments using the SAGE algorithm," *IEEE Journal on Selected Areas in Communications*, vol. 17, no. 3, pp. 434–450, 1999.
[19] M. S. Bartlett, "Smoothing Periodograms from Time-Series with Continuous Spectra," *Nature*, vol. 161, pp. 686–687, 1948.
[20] R. Schmidt, "Multiple emitter location and signal parameter estimation," *IEEE Transactions on Antennas and Propagation*, vol. 34, no. 3, pp. 276–280, 1986.
[21] R. Roy and T. Kailath, "ESPRIT-Estimation of Signal Parameters Via Rotational Invariance Techniques," *IEEE Transactions on Acoustics, Speech, and Signal Processing*, vol. 37, no. 7, pp. 984–995, 1989.
[22] J. Ø. Nielsen, W. Fan, P. C. Eggers, and G. F. Pedersen, "A Channel Sounder for Massive MIMO and MmWave Channels," *IEEE Communications Magazine*, vol. 56, no. 12, pp. 67–73, 2018.